

**Predicting Convectively Induced Turbulence With Regionally
Convection-Permitting Simulations**

Haoming Chen^a, Christy Yan-yu Leung^b, Ping Cheung^b, Haolin Liu^a, Sai Tick Chan^b,
Xiaoming Shi^a

^a*Division of Environment and Sustainability, Hong Kong University of Science and Technology,
Hong Kong, China*

^b*Hong Kong Observatory, Hong Kong, China*

Corresponding author: Xiaoming Shi, shixm@ust.hk

9 ABSTRACT: Convectively induced turbulence (CIT) is a severe aviation hazard. It is challenging
10 to forecast CIT because low-resolution models cannot explicitly resolve convective motions at
11 kilometer scales. In this study, we used the Model for Prediction Across Scales (MPAS) to
12 simulate CIT cases with convection-permitting resolution in the region of the CIT events and
13 coarse resolution in other parts of the globe. We developed a new method to compute the eddy
14 dissipation rate (EDR) from the velocity field simulated by MPAS. It is based on explicit filtering
15 and reconstruction in large-eddy simulations and estimates turbulence kinetic energy (TKE), which
16 is then used to calculate EDR. The new method's performance is better than previous methods
17 based on second-order structure functions and convective gravity wave drag regarding the predicted
18 turbulence intensity and spatial distribution. It also has better performance in distribution of EDR
19 and higher correlation coefficient with observations. A higher resolution (1 km) generates more
20 intense EDR and improved spatial pattern but is also computationally demanding. 3-km resolution
21 is a balance considering the trade-off between accuracy and cost. Because convection-permitting
22 resolutions are in the gray zone for simulating convection, we evaluated the sensitivity of the
23 prediction to the variations of physical and numerical schemes. Varying cumulus convection
24 parameterization and numerical monotonic flux limiter are identified to be effective approaches to
25 generating beneficial ensemble spread. However, a physical perturbation-based ensemble still has
26 limitations in generating enough ensemble spread.

27 SIGNIFICANCE STATEMENT: Aviation turbulence poses risks to flight passengers and crew,
28 but it is difficult to predict when caused by convection. Because high resolutions are required
29 in numerical models to fully resolve convective motions. Kilometer-scale resolution can at least
30 partially resolve convection; therefore, numerical models at such resolutions are a promising tool
31 for predicting aviation turbulence. Here, we developed a new method to compute turbulence based
32 on kilometer-scale resolution simulations. The method provides more accurate intensity and spatial
33 pattern prediction than previous methods. It also has better performance in statistics characteristics.

34 1. Introduction

35 Aviation turbulence is the primary weather-related factor contributing to aviation incidents,
36 causing numerous injuries, occasional fatalities, and structural damage each year. Furthermore,
37 schedule delays, air traffic management problems and operational costs to airlines are usually
38 resulted by turbulence (Tvaryanas 2003; Sharman et al. 2012; Kim and Chun 2016; Sharman and
39 Lane 2016). Convectively induced turbulence (CIT) is a type of aviation turbulence and a challenge
40 for aviation safety. CIT can be generated from the following physical mechanisms 1) convection
41 which penetrates the upper troposphere can enhance the background wind shear, 2) cloud-induced
42 deformation at the cloud boundary caused by buoyancy gradients, and 3) gravity waves generated
43 from convection break above convection (Lane et al. 2003). To forecast CIT, atmospheric models
44 are used to simulate the relevant weather conditions. Many turbulence prediction products rely on
45 empirical indices related to measures of gravity waves or atmospheric instability (Endlich 1964;
46 DUTTON 1980; Vogel and Sampson 1996; Ellrod and Knox 2010; Muñoz-Esparza and Kosović
47 2018).

48 When atmospheric models are used to forecast turbulence, the model resolution is a critical
49 barrier. Convection permitting (~ 1 km) resolution can help a model explicitly simulate convection,
50 but its computational cost is expensive. Additionally, in the atmosphere, eddies span a spectrum of
51 sizes from 100 kilometers down to centimeters, but aircraft bumpiness is most pronounced when
52 the size of the turbulent eddies encountered is about the size of the aircraft (Vinnichenko 2013).
53 For commercial aircraft, this would correspond to eddy sizes on the order of 100 m, which is
54 infeasible for operational numerical weather prediction (NWP) models.

55 Previous studies have developed practical algorithms to forecast non-convectively induced tur-
56 bulence. Sharman et al. (2006) developed the Graphical Turbulence Guidance system, version 2
57 (GTG2), to forecast aviation turbulence with the input data which are generated by an NWP model
58 with a 20-km horizontal resolution. GTG2 utilizes numerous turbulence diagnostics with improv-
59 ing forecast quality, and it is recognized that NWP model resolution is one factor that hampers more
60 accurate results. In its latest version (GTG3), Sharman and Pearson (2017) used a 13-km resolution
61 results from Weather Research and Forecasting Rapid Refresh and acknowledged the necessity for
62 higher resolutions (grid spacing less than 3 km or 1 km) for some upper-level turbulence events. In
63 addition, GTG3 was also applied in higher resolution (3 km) and machine learning was applied to
64 improve the EDR forecast in distinguishing (Muñoz-Esparza et al. 2020). The Korean Integrated
65 Turbulence Forecasting Algorithm (KITFA) is a product similar to GTG2, and it uses the results
66 of 30-km resolution simulations to provide turbulence intensity forecasts. It performs well for the
67 turbulence due to jet streams, specifically for clear air turbulence (CAT), but for CIT, it does not
68 have any metrics (Jang et al. 2009).

69 High-resolution simulations have been employed in research to study CIT, showing promising
70 results. Barber et al. (2019) used the Weather Research and Forecast (WRF) model with nested
71 domains to capture the turbulence in the Gulf of Mexico, and their finest resolution is 3 km. The
72 simulation utilized in Barber et al. (2019) captured CIT successfully and showed that developing
73 convection can generate more substantial turbulence than mature convection. Lane and Sharman
74 (2014) used a large-eddy simulation with 75-m resolution in the horizontal. They found the position
75 of the strongest turbulence is outside of convective clouds, and CIT extends to 50 km away from
76 the cloud boundary, beyond the Federal Aviation Administration (FAA) guidelines. Other studies
77 also found that the higher resolution models can help us understand the life cycle of CIT (Lane
78 et al. 2009; Trier et al. 2010; Trier and Sharman 2016).

79 The eddy dissipation rate to the one-third power (EDR, unit: $\text{m}^{2/3}\text{s}^{-1}$) is valuable for comparing
80 high-resolution model prediction and observed aviation turbulence. EDR has been adopted as
81 a significant turbulence indicator reported by the International Civil Aviation Organization. It
82 represents the kinetic energy transfer rate from large-scale eddies to small-scale ones Sharman
83 and Pearson (2017). The previous studies commonly used the second-order structure functions
84 to calculate EDR from high-resolution model output, which is a very useful statistic created by

85 Kolmogorov and measures the kinetic energy of all vortex structures with a given scale (Kolmogorov
86 1991; Frehlich and Sharman 2004; Sharman et al. 2006). The calculation of EDR from second-
87 order structure functions (2ndSF) on the mesh is a well-established technique, and some studies
88 have calculated best-fit functions based on a statistical analysis of physical quantities in the middle
89 and upper atmosphere, such as wind speed, pressure and potential temperature (Frehlich and
90 Sharman 2004, 2010; Lindborg 1999). Barber et al. (2019) used the turbulence kinetic energy
91 (TKE) from the planetary boundary layer scheme to compute EDR and made a comparison with
92 the result from the 2ndSF. They suggest that the 2ndSF is more useful. Convective gravity wave
93 drag (CGWD) can also be used to calculate the EDR by estimating the impact due to gravity wave
94 breaking (Kim et al. 2019).

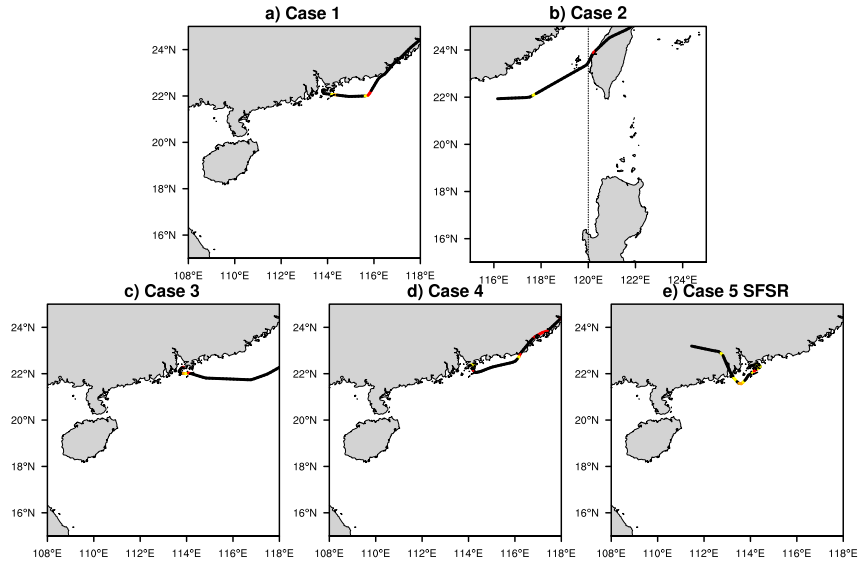
95 In this research, we evaluate the potential of the Model for Prediction Across Scales (MPAS) in
96 predicting CIT with several reported incidents near Hong Kong. Section 2 lists the details of the
97 incidents, configurations of the model, and methods to estimate EDR. A new method to estimate
98 EDR based on subfilter-scale reconstruction(SFSR) (Chow et al. 2005) is described. Section 3
99 shows the performance of MPAS in simulating convection. Different EDR estimation methods
100 and the influence of resolution are presented in section 4. Section 5 discusses the influence of
101 different physical parameterization or numerical options might change the convection. Section 6
102 evaluates the performance of those methods with more cases and discusses more specific properties
103 in statistics between these methods.

104 **2. Experimental Design and Methods**

105 *a. MPAS Setup*

106 This study used MPAS version 7 to conduct convection-permitting simulations. MPAS features
107 a non-hydrostatic dynamical core that utilizes unstructured Voronoi meshes and C-grid discretiza-
108 tion (Skamarock et al. 2012). The global variable-resolution mesh can have finer resolutions in
109 interested areas. In recent years, MPAS has extensive application in investigating various signifi-
110 cant scientific issues dependent on resolution, including clouds, extreme precipitation events, and
111 atmospheric rivers. (O’Brien et al. 2013; Landu et al. 2014; Yang et al. 2014; Hagos et al. 2015;
112 Sakaguchi et al. 2015; Zhao et al. 2016).

113 This study focuses on five severe CIT incidents reported near Hong Kong. Table 1 lists the
114 time, altitudes, and objective observations, in-situ EDR (Takacs et al. 2005) for those cases. EDR
115 and location data were recorded by aircraft, and shown in Fig. 1. Unless specified otherwise,
116 our numerical experiments are conducted with a 3 ~ 60 km mesh. Figure 2 b shows the mesh
117 configuration, which has a 3-km resolution in South China and the South China Sea and a transition
118 to a 60-km resolution away from this region. To examine the impact of resolution on the results of
119 this study, other refined resolutions, 1 km, 9 km, and 18 km, are used for the refined region in some
120 simulations (Fig. 2).



121 FIG. 1. Trajectories and turbulence from different cases in Table 1. a) Case 1, b) Case 2, c) Case 3, d) Case
122 4 and e) Case 5. The line represents the route of the airplanes, while red indicates the EDR ($\text{m}^{2/3}\text{s}^{-1}$) is higher
123 than 0.3, orange for 0.2–0.3, yellow for 0.1–0.2, black for 0–0.1.

TABLE 1. Time (UTC), altitude, flight stage, and maximum turbulence intensity of the five CIT cases.

Case	Time	Altitude (m)	Stage	Max EDR ($\text{m}^{2/3}\text{s}^{-1}$)@Time
1	2020-05-21	10000	cruising	0.465@01:49
2	2020-06-06	9450	cruising	0.623@09:35
3	2020-06-08	4500	landing/taking off	0.493@04:24
4	2020-08-26	6600	cruising	0.687@13:27
5	2021-06-27	3900	landing/taking off	0.516@23:48

124 The model is configured to have 55 vertical layers, with the top of the model at 22 km above the
 125 surface. The “Base” experiment uses the Grell-Freitas (GF) convection parameterization, which
 126 is modified to work across grid spacings from mesoscale to convective scales (Grell and Freitas
 127 2014), the MPAS microphysics suite, which uses the Thompson scheme (Thompson et al. 2008)
 128 for grid cells smaller than 10 km and the WSM6 scheme (Hong et al. 2006) for other cells, the
 129 planetary boundary layer scheme suite, which uses the YSU (Hong 2010) at the coarser resolution
 130 and the MYNN (Nakanishi and Niino 2009) at the finer resolution. The Noah land surface scheme
 131 (Chen and Dudhia 2001), and the RRTMG short and longwave radiation schemes (Mlawer et al.
 132 1997; Iacono et al. 2000) are used in all simulations.

133 Because the convection-permitting resolution is in the gray zone for convection, the choices
 134 of relevant parameterization are subject to uncertainty. Therefore, we evaluate the potential of
 135 physics-based ensembles by varying physical or numerical options, one at a time, in our simulations.

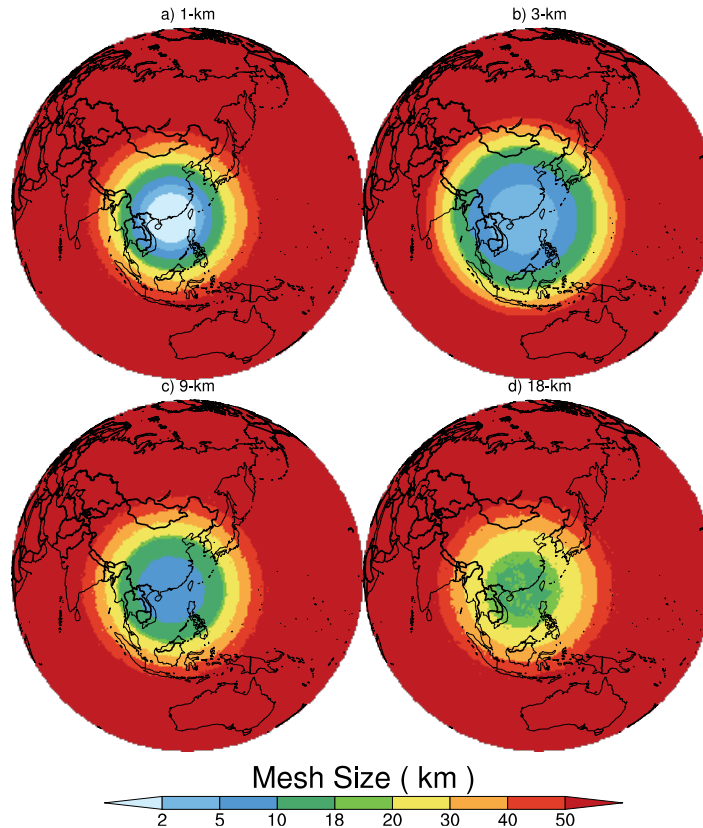


FIG. 2. Global variable-resolution mesh size in the variable-resolution a) 1 ~ 60 km, b) 3 ~ 60 km, c) 9 ~ 60 km, and d) 18 ~ 60 km experiments.

Table 2 lists the difference between each experiment and the “Base” run. We varied the choices for microphysics which has influence on hydrometeors as well as the convection (Mohan et al. 2019); cumulus convection parameterization since we have high resolution to simulate the convection directly; monotonic limiter in scalar advection, turning it off may cause instability in small area; and the Smagorinsky coefficient which can influence the turbulent viscosity for horizontal turbulence mixing. SMAG-S and SMAG-L represent two experiments with small (0.025) and large (0.5) Smagorinsky coefficients. Overall, in gray zone, the selections of those schemes are controversial and can influence small-scale motions, which impact the estimation of EDR.

TABLE 2. Model parameterizations used in simulations. Each member has one modification in options compared to “Base”.

Experiments	Physics/Numerics	Default options (“Base”)	Experiment choice
WSM6	Microphysics	Thompson	WSM6
NoCU	Cumulus convection	Grell-Freitas	None
NoML	Monotonic limiter	On	Off
SMAG-S	Smagorinsky coefficient	0.125	0.025
SMAG-L	Smagorinsky coefficient	0.125	0.5

The initial conditions are derived from the European Centre for Medium-Range Weather Forecast (ECMWF) fifth-generation reanalysis (ERA5) data at a 0.25° horizontal grid spacing and 37 vertical levels (Bell et al. 2021). We additionally conducted initial-condition-based ensemble simulations in the later part, the ensemble members are generated by adding different random perturbations sampled from a Gaussian distribution with a mean of zero and a variance equal to the expected variances of the observation errors (Hersbach et al. 2020). The perturbed initial conditions are from ten ERA5 ensemble members. The initialization time of our simulations is approximately 12 hours before the occurrence of the maximum CIT in each case. We tested experiments with initialization six hours before the CIT incidents, but those simulations produced less accurate predictions, which probably resulted from the need for model spinup.

b. Calculation of EDR

Here, we briefly describe the three methods to compute EDR, which we compared in this study. They are based on (1) second-order structure function, (2) subfilter-scale reconstruction, and (3)

convective gravity wave drag (CGWD). The second one is the new method we developed in this study.

1) SECOND-ORDER STRUCTURE FUNCTIONS

In this method, turbulence can be described by longitudinal and transverse structure functions, which are defined by

$$D_{LL}(r) = \langle [u_L(x) - u_L(x+r)]^2 \rangle \quad (1)$$

$$D_{NN}(r) = \langle [u_N(x) - u_N(x+r)]^2 \rangle \quad (2)$$

respectively. They measure the kinetic energy of all vortex structures with a scale less than or equal to the length r . Here the u_L is the velocity component along the position vector $\mathbf{r} = (x, y, z)$, and u_N is the transverse component, r is a separation distance expressed in units of spatial grid steps, and the angle brackets indicate the average in a spherical surface with radius $|\vec{r}|$. In Kolmogorov's model, based on universal equilibrium hypotheses, when the length scale is in the inertial subrange, the structure functions and EDR can be linked by

$$D_{LL}(r) = C_k \varepsilon^{2/3} r^{2/3} \approx 2 \varepsilon^{2/3} r^{2/3} \quad (3)$$

$$D_{NN}(r) = \frac{4}{3} C_k \varepsilon^{2/3} r^{2/3} \approx \frac{8}{3} \varepsilon^{2/3} r^{2/3} \quad (4)$$

where C_k is set to 2 and $\varepsilon^{1/3}$ is the EDR. The difference in the coefficients in two directions is deduced by Monin and Yaglom (2013). In our calculation, r is seven grid spacings because it should represent the spectral resolution of the advection scheme which is 7~10 Δx (Skamarock 2004; Muñoz-Esparza et al. 2018; Barber et al. 2019).

For the resolution of convection-permitting simulations, it is difficult to apply the same horizontal separation length (in our mesh, 30 km) to the vertical because of the relatively shallow depth of the troposphere. Many previous studies consider the horizontal velocities and gradients only to calculate the structure functions (Barber et al. 2019; Frehlich and Sharman 2004), and this approximation is also what we adopted here.

183 2) SUBFILTER-SCALE RECONSTRUCTION

184 This method estimates EDR by computing TKE first. Here, we adopt the idea of explicit filtering
 185 and reconstruction in the parameterization of turbulence (Chow et al. 2005). In this framework,
 186 subfilter scales are separated into resolvable subfilter scales (RSFS) and subgrid scales (SGS). The
 187 RSFS components have much more energy than the SGS component. Thus, we compute the RSFS
 188 part only. Following Chow et al. (2005), we first reconstruct RSFS velocity through deconvolution.
 189 The reconstructed RSFS velocity

$$\widetilde{u}_i^* = \overline{\widetilde{u}_i} + (I - G)\overline{\widetilde{u}_i} + (I - G)(I - G)\overline{\widetilde{u}_i} + \dots \quad (5)$$

190 where the overline denotes the filter, the tilde denotes discretization, $\overline{\widetilde{u}_i}$ is, therefore, the grid
 191 variable from MPAS, I is the identity operator, and G is the filter. In this study, the filter is a
 192 top-hat filter (1-2-1 filter) applied to all three dimensions. The corresponding cutoff wavelength
 193 is $2\Delta x$. This filter is the recommendation from (Chow et al. 2005; Gullbrand and Chow 2003)..
 194 Keeping $\overline{\widetilde{u}_i}$ is the zero-order reconstruction and is what we adopted. Including more terms on the
 195 right side of Eq. 5 generates higher-order reconstruction, which is not used in this study because it
 196 may occasionally generate negative TKE.

197 After obtaining RSFS velocities, the RSFS TKE is

$$\text{TKE} = \frac{1}{2} \left(\overline{\widetilde{u}_i^* \widetilde{u}_i^*} - \overline{\widetilde{u}_i}^* \overline{\widetilde{u}_i}^* \right) \quad (6)$$

198 Assuming the turbulence is in the inertial subrange, the EDR is the following (Schumann 1991),

$$\varepsilon^{1/3} = \left(\text{TKE}^{3/2} / L \right)^{1/3} \quad (7)$$

199 where $L = (\lambda \Delta x \Delta y \Delta z)^{1/3}$ is the integral scale of the turbulence, Δx , Δy and Δz are grid spacings. In
 200 our calculations, MPAS data were interpolated to $0.04^\circ \times 0.04^\circ$ rectangular grid before applying the
 201 above equations by using Earth System Modeling Framework library through the NCAR Command
 202 Language (Brown et al. 2012) with “bilinear”, which is widely used in MPAS hexagon mesh (Li
 203 et al. 2022; Mingyue et al. 2021). Therefore, Δx and Δy are approximately 4.5 km for the region
 204 near Hong Kong, and Δz is 500 m, which is the grid spacing in the middle troposphere. λ is a flow

dependent quantity and complex to obtain (Barber et al. 2019; Sharman et al. 2012). This value can be calculated from boundary layer parameterization schemes (Ahmad and Proctor 2012), but this method does not work in our high-altitude cases. We acknowledged that this problem is difficult to solve immediately, and we selected a constant value, $\lambda = 8$, for our calculation because of the cutoff wavelength ($2\Delta x$) in our filter.

Applying filters on the original MPAS grid is also possible. Allen (2005) developed filters for hexagonal grids. Our evaluation found using the filtering technique described in Allen (2005) yields results similar in spatial distribution and magnitude to our calculation using data interpolated to the latitude-longitude grids (See Appendix A). However, due to regional refinement, MPAS mesh has some grid cells with five or seven edges, which requires some modification of the filters by Allen (2005); this problem becomes more severe in coarser mesh such as 9 ~ 60 km mesh.

3) CGWD-BASED ESTIMATION

CGWD parameterization was used by Kim et al. (2019) to calculate EDR. However, MPAS only has a parameterization for gravity wave drag due to orography. To compare the reconstruction method results with CGWD-based estimation, we use RSFS reconstruction to estimate the momentum flux in the model, e.g.,

$$\tau_{13} = \overline{\widetilde{u}_1^* \widetilde{u}_3^*} - \overline{\widetilde{u}_1^*} \overline{\widetilde{u}_3^*} \quad (8)$$

Then the CGWD can be given by the divergence of momentum flux,

$$\text{CGWD} = \frac{1}{\rho} \frac{\partial \rho \tau_{13}}{\partial z} \quad (9)$$

and the diffusion coefficient is

$$K_{\text{CGWD}} = \left| \text{CGWD} \frac{c - U}{N^2} \right| \quad (10)$$

where c is the horizontal phase speed, which is set to zero by assuming that CGW is stationary relative to the convections, U is the base-state wind, N is the Brunt-Väisälä frequency, and ρ is the density of the air. The TKE in this method is

$$\text{TKE} \approx \left(C_d^{-1} \frac{K_{\text{CGWD}}}{L} \right)^2 \quad (11)$$

226 and the EDR is

$$\text{EDR} \approx \left(\frac{C_\varepsilon \text{TKE}_{\text{CGWD}}^{3/2}}{L} \right)^{1/3} \quad (12)$$

227 where C_d is set to 0.1 and the C_ε is set to 0.93.

228 3. Large-scale Environmental Conditions

229 Figure 3 shows the areal coverage of brightness temperature for Case 1 (Table 1) in an infrared
230 channel of Himawari-8 satellite observation and the experiments with different physics or numerics
231 options (Table 1), the multi-scale structural similarity (MSSSIM, a higher value close to 1 indicates
232 higher similarity between the two images) is used to compare the similarity between experiments
233 and observation. The MSSSIM values are shown in respective titles and higher values mean higher
234 similarity. The brightness temperature for model data is simulated with the Radiative Transfer for
235 TOVS (RTTOV). The overall spatial distribution of clouds is similar in those simulations, with
236 one intense convective system in the northern part of the South China Sea and another overland
237 in the Guangdong province of China. However, comparing the Base run and satellite images, we
238 can find that the pattern of the over-land convection is not the same. In the satellite image, there
239 is a gap (clear-sky area) between the convective systems over land and over ocean, but in Base
240 simulation, the two are partially connected, and clouds partially cover the coastal line. NoCU
241 simulation appears to be the only one exhibiting clear-sky conditions along the coastal line, but
242 there is a deviation between NoCU and observation in this clear-sky area, so its MSSSIM is not
243 the highest. WSM6 displays notably higher cloud tops and less anvil cloud, so it has the lowest
244 MSSSIM, and the value is significantly different from the other five experiments. The other three
245 simulations, NoML, SMAG-S, and SMAG-L, appear to have minimal changes to the Base due to
246 their influences are at small scales, at least for this case and the infrared channel.

247 Overall, compared to satellite data, all six experiments have effectively simulated the location
248 and intensity of convection at large scales without any significant biases. Based on this, we will
249 continue to discuss their results regarding turbulence.

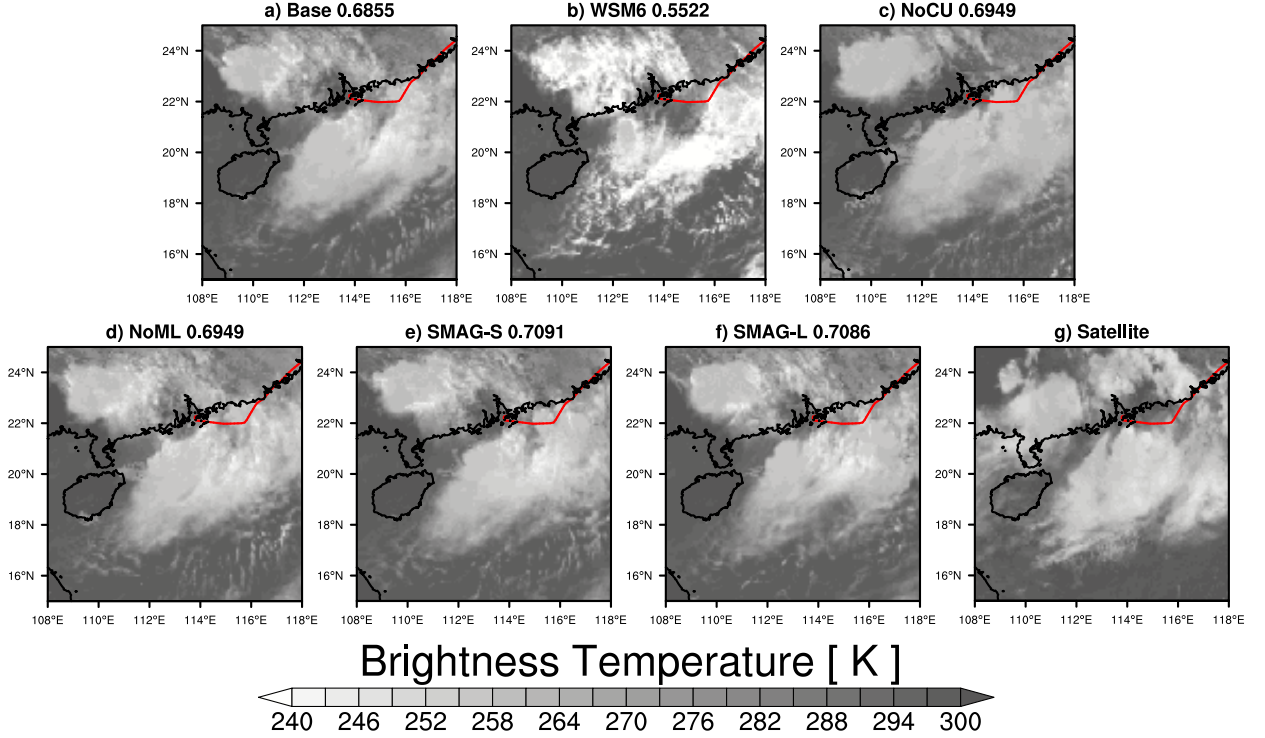


FIG. 3. Spatial distributions of the brightness temperature simulated by RTTOV for different experiments and observed by Himawari-8 for its Channel 7 on May 21, 2020, at 01:50 UTC and their corresponding MSSSIM values to observation. (a) Base, (b) WSM6, (c) NoCU, (d) NoML, (e) SMAG-S, (f) SMAG-L, and (g) satellite observation. The red line represents the route of the airplane in Case 1 in Table 1, the details about the turbulence are in Fig. 1.

4. EDR Estimation in Convection-Permitting Simulations

In this section, we evaluate the performance of different EDR estimation approaches for convection-permitting simulations of the cases (Base run) listed in Table 1.

Figure 4 shows the results from the three methods and that from GTG3, which uses several indices related to upper-level turbulence such as Frontogenesis function (isentropic coordinates) / Ri (Richardson Number), $|Deformation|^2/Ri$ (Sharman et al. 2006) and a dynamic weighting method to them to obtain a comprehensive forecast, the data source is from the World Area Forecast System (WAFS) from National Weather Service, United States with the resolution of 0.25° . Data at 00:00 UTC on May 21, 2020, are used because the closest GTG3 prediction is at 00:00.

Although all three methods predict significant turbulence at the location of the CIT incident (red segment of the flight trajectory in Fig. 4), the result based on the 2ndSF (Fig. 4b) underestimates

turbulence intensity, while that based on CGWD (Fig. 4c) overestimates. The SFSR method (Fig. 4a) yields the EDR most close to observation. Compared with GTG3 prediction, 2ndSF and CGWD underestimate the spatial coverage of high EDR area, especially for the southeast quadrant of the plotted domain. Therefore, the SFSR is more accurate because it has higher probability of detection. In addition, the separation in 2ndSF may be below the effective resolution of MPAS due to the implicit diffusion of the advection scheme and other explicit filters (Skamarock et al. 2014). Therefore, we also did sensitivity tests on the separation length of the 2ndSF. The spatial distributions of the EDR with the variations of separation lengths from $7\Delta x$ to $15\Delta x$ in 3 km mesh have similar large-scale patterns. In this case, linear regression may be a potentially better method. In this plotted region, there is a linear relationship between the average value of the second-order structure functions and the separation length. However, drastic numerical changes in each cell can lead to many negative values and overestimation. Thus, we continue to use a separation length of $7\Delta x$ for our 2ndSF calculations.

Because the SFSR method relies on resolved velocities, it is necessary to examine what resolution is sufficient for the EDR estimation. The procedures of calculations are identical in different resolutions, while the integral scale, L , should be calculated based on the resolution. Figure 5 shows the spatial distributions of EDR calculated from the simulations with different resolutions in the refined region, from 1 km to 18 km. Those results exhibit a remarkable difference in EDR intensities, with the 1-km mesh simulation showing stronger turbulence and the 18-km mesh simulation showing the smallest EDR values. It is tempting to suggest those differences in intensity can be calibrated by adjusting the factor λ above, but careful examination reveals that such tuning would not yield the same EDR pattern. For instance, in Fig. 5a, the high EDR region in the southeast quadrant is organized in a triangular shape with some wave patterns, but in Fig. 5d, the high EDR values found in the southeast quadrant are line-shaped. Meanwhile, we evaluated the performance of the 2ndSF method at different resolutions. The 1-km mesh can also have higher values, and underestimation and deviations are observed in the inland area on 9-km and 18-km meshes. The different values at different resolutions also remind us that the turbulence intensity thresholds other researchers used previously (Sharman and Pearson 2017), defining 0.15~0.22 as light, 0.22~0.34 as moderate, and >0.34 as severe. However, based on observations, it is due to the that the medium-sized aircraft always fly the routes between Hong Kong and adjacent areas such

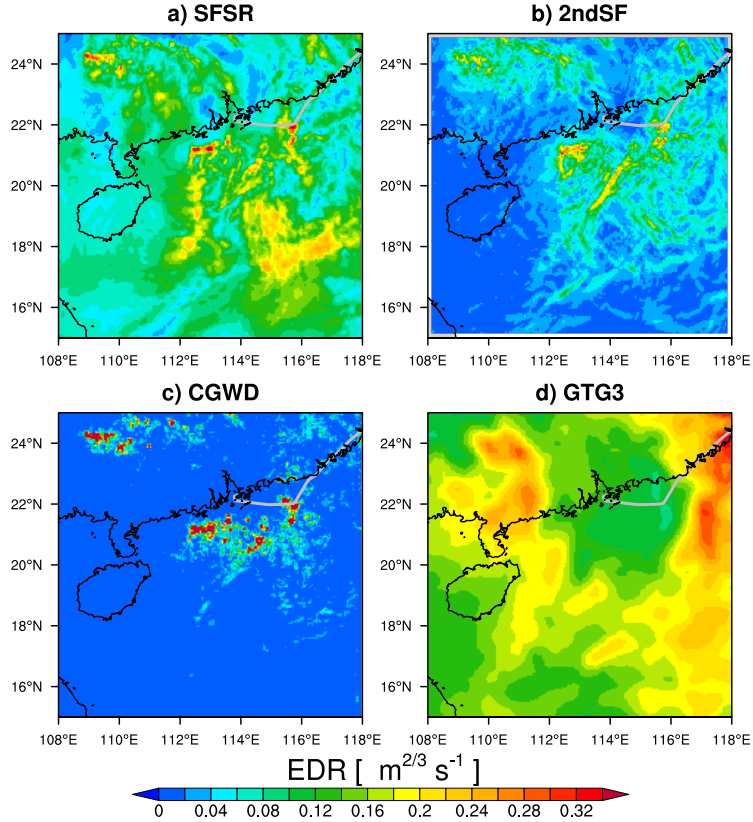


FIG. 4. Spatial distributions of the EDR calculated with different methods at the altitude of 10 km, on May 21, 2020, at 00:00 UTC. (a) is based on the subfilter-scale reconstruction, (b) second-order structure functions, (c) CGWD, and (d) GTG3 Forecast, 27 km. The lead time of GTG3 forecast is 12 hours. The source of the data is <https://www.aviationweather.gov/wifs/products>. The line represents the trajectory of the airplane in Case 1 listed in Table 1. The gray line represents the route of the airplane in Case 1 in Table 1, the details about the turbulence are in Fig. 1.

as Taipei, light turbulence is considered to occur when the EDR reaches 0.1 (Sharman et al. 2014). Therefore, we have modified light turbulence to 0.1~0.22. These thresholds need to be adjusted in different resolutions, or our EDR results need to be calibrated. We need to get enough data to do the mapping or calibrations in the next project.

Although the EDR calculation yields results closer to observations at the 1-km resolution in this case, it demands much more computational resources (Table 3). In our 1-km resolution simulation, integrating one-time step (6 seconds model time) takes about 12 seconds wall-clock time when using 480 cores, and writing the large output file is equally time-consuming. The resulting wall-clock time for integrating MPAS for one hour and saving output is two and a half hours. By

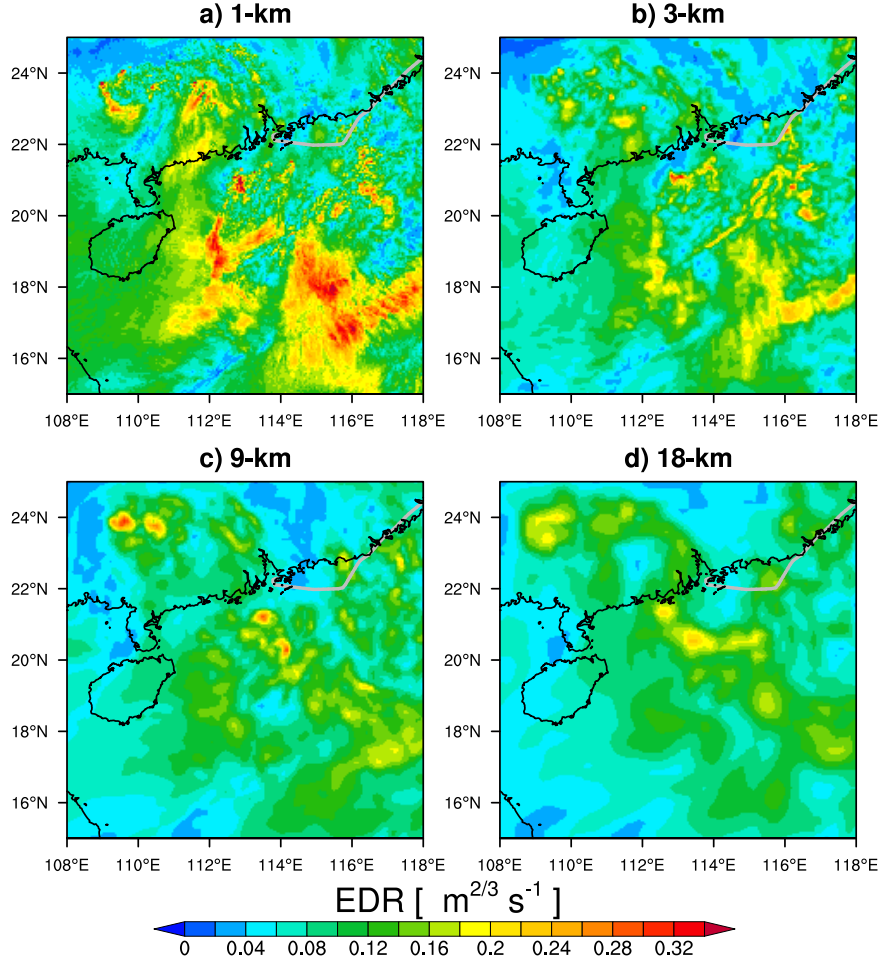


FIG. 5. Spatial distributions of the EDR at the altitude of 10 km, on May 21, 2020, at 01:50 UTC, calculated with the subfilter-scale reconstruction method for MPAS simulations with different resolutions: (a) 1 ~ 60 km, (b) 3 ~ 60 km, (c) 9 ~ 60 km, and (d) 18 ~ 60 km. The gray line represents the route of the airplane in Case 1 in Table 1, the details about the turbulence are in Fig. 1.

contrast, the 3-km resolution simulation takes only 15 minutes wall-clock time for the same task when using only 240 cores.

TABLE 3. Computational resources consumption for 15 hours model time integration using different MPAS meshes

Meshes(km)	Cells	Cores	Time (min)
1 ~ 60	2,827,196	480	890
3 ~ 60	835,586	240	210
9 ~ 60	293,533	240	37
18 ~ 60	207,915	240	29

5. Sensitivity to Gray Zone Related Parameterizations

Because the limited predictability of convection implies the need for ensemble forecast, here we evaluate how sensitive the CIT prediction is to the variation of physics and numerics, which arguably represent potential sources of uncertainty other than initial conditions (Bouttier et al. 2012). Previous studies indeed suggested that in the gray zone, turbulence and convection representations could significantly change the development and intensity of convection (Shi et al. 2019; Shi and Wang 2022).

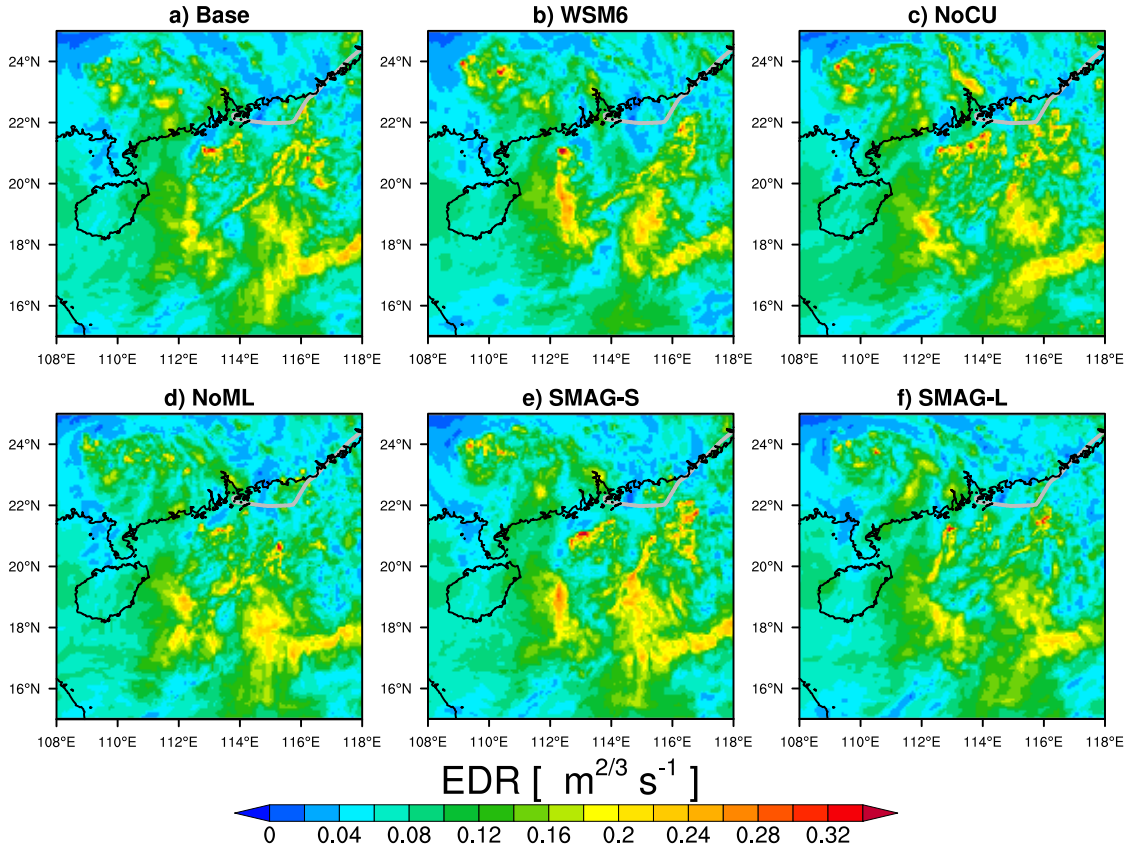


FIG. 6. Spatial distributions of the EDR calculated on different experiments at the altitude of 10 km, on May 21, 2020, at 01:50 UTC (a) Base, (b) WSM6, (c) NoCU, (d) NoML, (e) SMAG-S and (f) SMAG-L. The EDR here is calculated with the subfilter-scale reconstruction method. The gray line represents the route of the airplane in Case 1 in Table 1, the details about the turbulence are in Fig. 1.

Figure 6 shows the spatial distribution of the EDR for Case 1 in those different experiments, with the EDR calculated using the subfilter-scale reconstruction method. WSM6 simulation exhibits more intense turbulence at some locations but an overall pattern differing from other simulations.

334 In the southeast corner of different simulations, there is a southwest-northeast oriented band of
335 high EDR, but in the WSM6 run, this band is much smaller and weaker. Though having a pattern
336 similar to most others, SMAG-S exhibits higher EDR, probably because the smaller eddy viscosity
337 prevented strong dissipation due to the parameterized turbulence mixing. NoCU simulation exhibits
338 quite some localized regions of EDR maximum values near the coast, which match the airplane
339 report of the CIT incident better.

340 Figure 7 shows the evolution of horizontally averaged radar reflectivity factor in the whole plotted
341 domain to include active convection in this refined region. All experiments show the development
342 of convection to its strongest state and then gradually declining. WSM6 has an earlier triggering of
343 deep convection, and by 01:49 UTC on May 21, its convection has started decaying. The NoCU and
344 Base experiments show a later triggering convection and peaking in intensity, While the NoCU has
345 stronger convection. Therefore NoCU shows more intense turbulence near the coastline in Fig. 6.
346 WSM6 shows a significantly lower reflectivity factor and the convection occurs at lower heights,
347 which may be attributed to that WSM6 can underestimate precipitation particles by producing
348 higher melting level (Min et al. 2015). This can also explain why WSM6 has a lower brightness
349 temperature in Fig. 3 and produces larger clouds at higher altitudes (See Appendix B).

350 To further illustrate the intensity and evolution of deep convection and its influence on turbulence,
351 Figure 8 shows the horizontal distribution of vertical velocity and the time series of the area-
352 averaged EDR. Strong vertical velocity regions can indicate the location of strong convection, as
353 shown in Fig. 3, where a wide spatial distribution of strong convection is observed in the southern
354 waters of Hong Kong, which coincides with the turbulence distribution in Fig. 6. It is noteworthy
355 that in WSM6, a convection system that exists in both the Base and NoCU experiments is missing
356 within the blue box in Fig. 8b, and the corresponding turbulence spatial distribution is also absent.
357 In addition, in the EDR-time series plot in Fig. 8d, WSM6 reaches its peak value earlier. The
358 peaking time is consistent with the time of the strongest convection. The Base and NoCU also
359 have this property in peaking time. In terms of intensity, the results from Base and WSM6 are very
360 similar, while NoCU is significantly higher. This relationship of the magnitude is also consistent
361 with the intensity of convection. Finally, as for the southeastern part of this region, where there is
362 no strong convection, turbulence is still observed in Fig. 4a, indicating that our new method can
363 capture turbulence (100 ~ 200km) away from the convection.

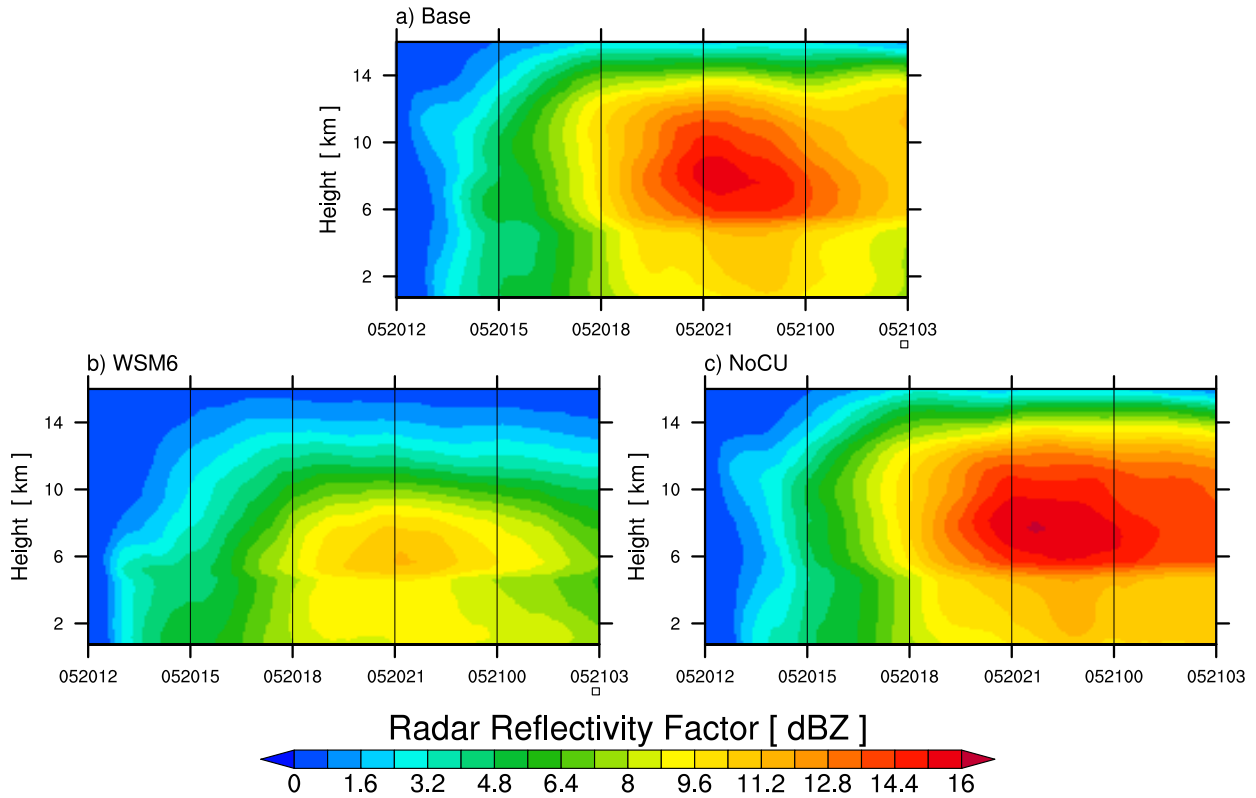


FIG. 7. Time series of radar reflectivity factor, averaged from 15°N to 25°N, 108°E to 118°E, from May 20, 2020, 12:00 UTC to May 21, 2020, 03:00 UTC, for a) Base, b) WSM6, and c) NoCU.

It is worth noting that the excessive cloud in WSM6 has an impact on practical CIT prediction. For aviation turbulence, it is crucial to identify the turbulence outside the clouds. Figure 8 e compares the fraction of out-of-cloud turbulence and Fig. B1 shows the height of clouds in these experiments. At lower altitudes, the cloud spatial distributions of the three experiments are consistent. However, at higher altitudes, the clouds in the other two experiments almost disappear, while in WSM6, they cover a larger area. This difference in cloud spatial distribution with height results in out-of-cloud turbulence dominating at upper levels, with a fraction close to 100% in the other experiments. In contrast, WSM6 simulation has only about 30% out-of-cloud turbulence at those levels. Thus, the choice of microphysics could produce not subtle but qualitatively different CIT prediction in operational use.

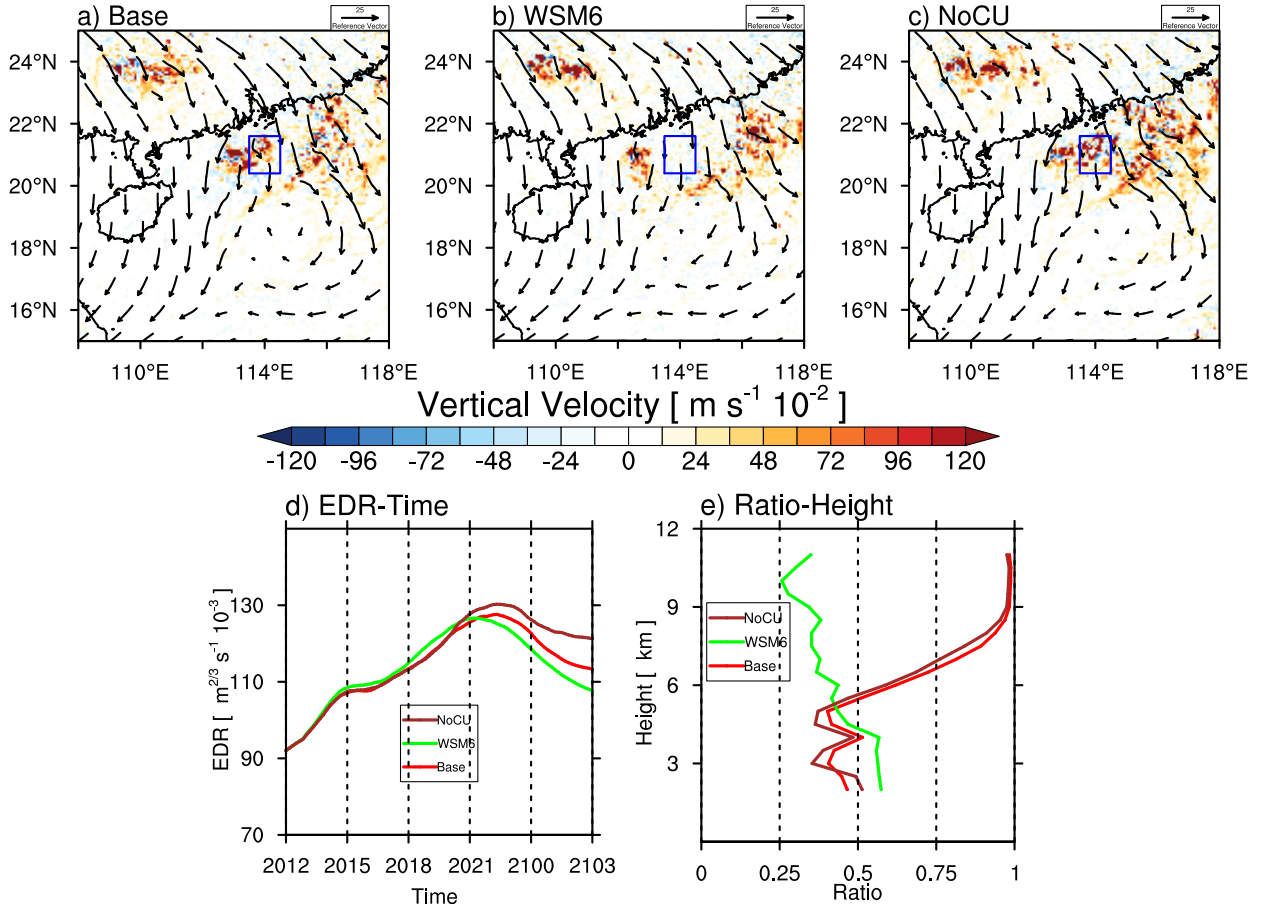


FIG. 8. Spatial distributions of the EDR at the altitude of 10 km, on May 21, 2020, at 01:50 UTC a) Base, b) WSM6, c) NoCU. d) Time series of EDR at the altitude of 10 km, averaged from 15°N to 25°N, 108°E to 118°E, from May 20, 2020, 12:00 UTC to May 21, 2020, 01:50 UTC. The numbers in the X axis represent the date and hour. e) Vertical profile of the ratio between the area of turbulence happens out of the cloud and the area of all the turbulence, including half an hour before and after the reporting time of Case 1. The thresholds of turbulence and cloud in e) are $0.10\text{m}^{2/3}\text{s}^{-1}$ of EDR and 10^{-5}kg/kg of cloud water mixing ratio and ice mixing ratio.

6. Evaluation With Other Cases

a. EDR Distribution of Five Cases

The reasonable prediction of CIT in Case 1 presented above is not necessarily generalizable because different convective systems have different predictability challenges. In Fig. 9, the EDR distribution along the flight route is shown for all the five cases listed in Table 2 and for the six experiments simulating each case with varied physics and numerics.

Firstly, the EDR data distributions of different methods are evaluated. CGWD exhibits excessively extremely high or low EDR values, which can easily lead to overestimation or underestimation.

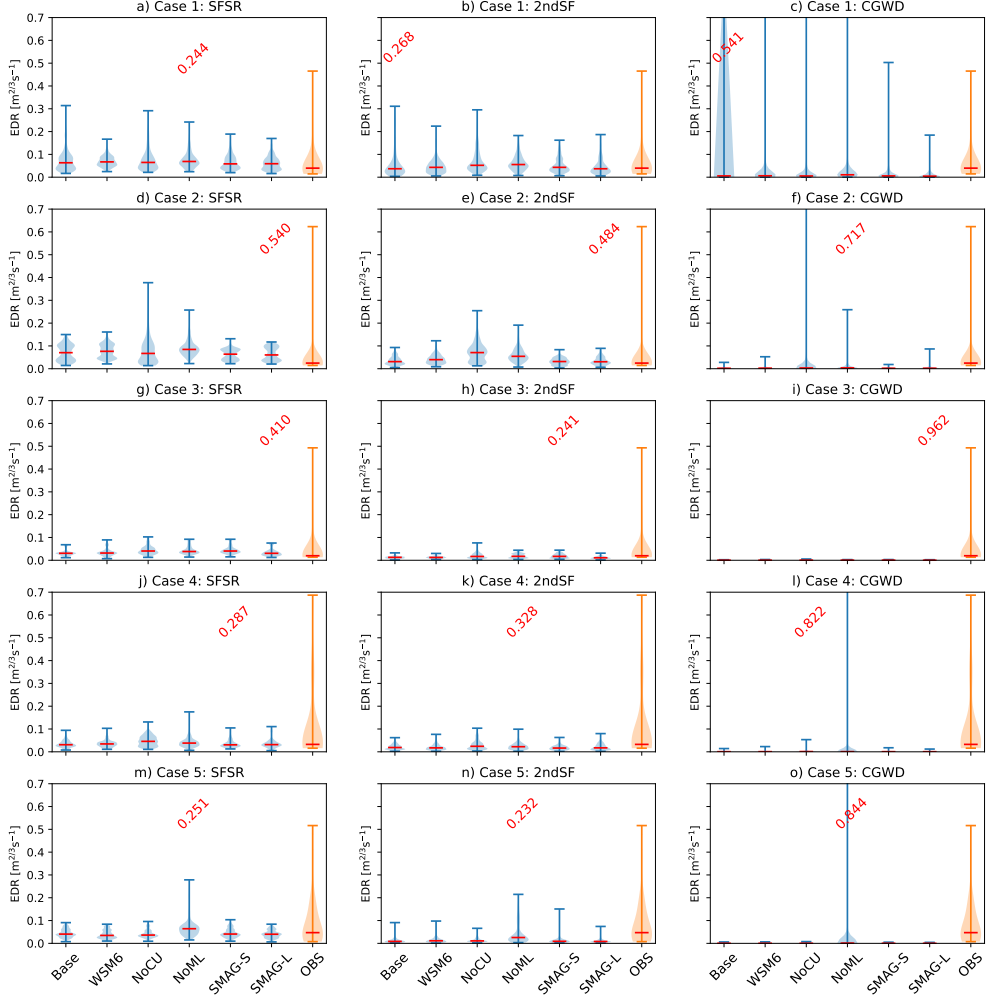


FIG. 9. Violin plot of the EDR within 10 km of the flight route in each case, including half an hour before and half an hour after the reporting time and collected according to airplanes' locations at the respective time. The rows correspond to the individual cases, from Case 1 to Case 5, while the columns represent the different methods, subfilter-scale reconstruction (SFSR), second-order structure functions (2ndSF) and CGWD. In a panel, Different positions represent different experiments with varied physics or numerics options. The observation distribution for the corresponding time is shown as the last box of each panel. The red horizontal line in a violin represents the median of EDR in experiments or observations. The red numbers above the violins are the greatest vertical distances from Kolmogorov-Smirnov Test between experiments and observations. Altitude change of airplanes is considered in the sampling.

Additionally, there is significant variation among different cases and members. For instance, in Fig. 9 o, only NoML exhibits a kernel density estimation (KDE) shape similar to the observations, while the EDR values for other experiments are close to zero. Regarding 2ndSF and SFSR, their KDEs resemble the observations, with a higher frequency of low EDR values and sporadic

401 high EDR values. These distributions are similar even for cases 3 and 4, where the forecasting
402 performance is not good. As for these poor performances in cases 3 and 4, it is not due to
403 the drawback of the methods themselves, instead, the errors are caused by biases in positions of
404 convection.

405 Overall, SFSR demonstrates better forecasting performance, exhibiting more similar KDE shapes
406 and more accurate maximum EDR values. The greatest vertical distances can reflect the effective-
407 ness of the SFSR by statistics. Some specific members and cases (NoCU, NoML in Case 1, NoCU
408 in Case 2, and NoML in Case 5) yield results closest to the observations with the SFSR method.
409 The greatest vertical distance in NoML in Case 5 is slightly lower than 2ndSF. However, it has a
410 closer maximum value of EDR to observation and more turbulence values, indicating the limitation
411 of the greatest vertical distance in evaluating the similarity of distributions. These experiments
412 outperform the results from 2ndSF with the same configurations.

413 As for the maximum EDR values in prediction, many simulations underestimate those observed
414 extreme values. The highest maximum EDR values are from NoCU, NoML, and Base. If we
415 compare those values with the observation, the prediction for maximum EDR appears acceptable
416 for Cases 1, 2, and 5, but substantial underestimation exists in the other two cases.

417 The overall estimation is, at least, partially due to the limited resolution. We have seen in Case 1
418 that increasing the refined region resolution to 1 km can significantly enhance the turbulence inten-
419 sity. NoCU usually exhibits stronger turbulence than others, probably because the GF convection
420 scheme, though scale-aware, still stabilizes the atmosphere too much and thereby weakens resolved
421 convective motions, lowering EDR estimation in the SFSR. NoML can also generate relatively
422 high EDR in some cases. The monotonic limiter helps advection schemes to avoid generating new
423 local extremes due to numerical errors, but it can also attenuate real extremes. Thus, turning it off
424 seems beneficial in some regimes.

425 *b. Distribution of EDR and thresholds*

426 Sharman and Pearson (2017) thinks that a lognormal distribution is essential for applying a
427 diagnostic to GTG3 and EDR should also be a lognormal distribution in the nature (Nastrom and
428 Gage 1985). Although there may still be bias because the results are from specific locations and
429 time (Sharman and Pearson 2017), we used the EDR results from 30 experimental results at all

altitudes and time points in the convection-permitting area to obtain distributions for SFSR and 2ndSF. Figure 10 shows that the results from SFSR and 2ndSF follow a lognormal right-skewed distribution. They have more values, which are higher than averages. The results of 2ndSF have smaller variance, with a peak probability exceeding 3%, but the overall value is lower than that of SFSR. The probability of numerical values below 0.1 is approximately 90% in SFSR. This probability is very close to previous statistics in North America from United Airlines and Delta Air Lines (Sharman et al. 2014). As for EDR higher than 0.5, the probability is 3×10^{-6} . This probability is one order of magnitude lower than the previous results (Sharman et al. 2014), indicating that for extreme turbulence, the EDR obtained based on the SFSR method with 3km mesh needs to be calibrated. The SFSR's probability density function shape is closer to the previous observation results (Sharman and Lane 2016). Although both methods have approximately a lognormal distribution, it is evident that SFSR has better statistical characteristics of EDR.

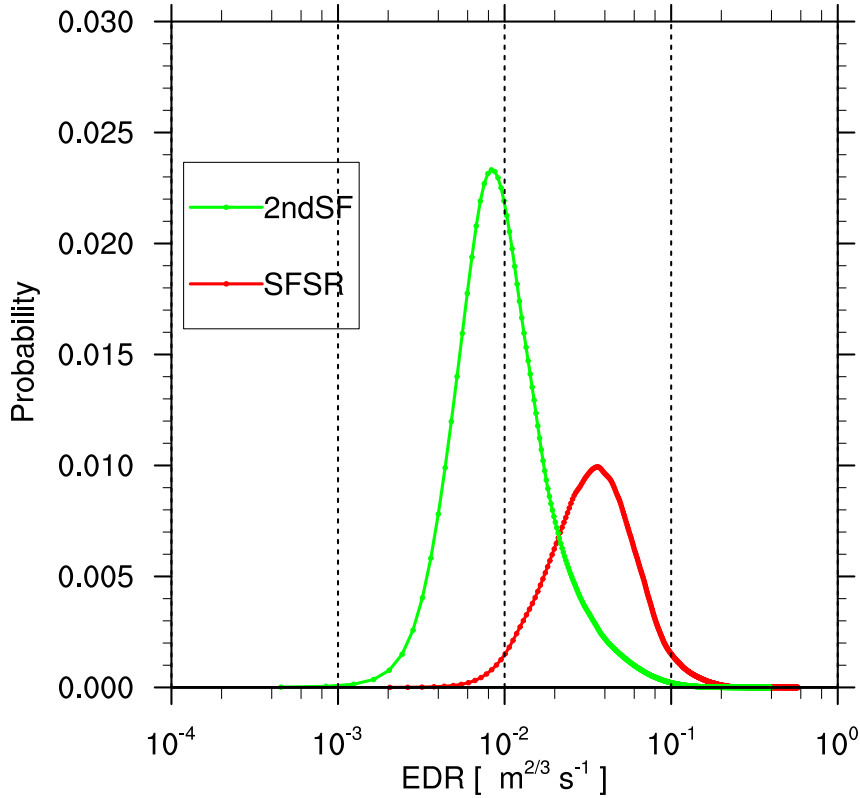


FIG. 10. Density plots of the EDR ($\text{m}^{2/3}\text{s}^{-1}$) from SFSR and 2ndSF. The data is from all experiments, from 15°N to 25°N , 105°E to 125°E and all altitudes. Three orange lines represent the thresholds: 0.1, 0.22, and 0.34.

442 *c. Probability of Detection and False Alarms*

443 The probability of Detection (POD) and False Alarms rate (FAR) are significant in evaluating a
444 prediction method. To further explain the superiority of SFSR, we conducted a scatter plot between
445 EDR data using different methods and observations. Muñoz-Esparza et al. (2018) indicated
446 skilled pointwise forecasts are not expected from NWP. Since we have high-resolution mesh and
447 observations have limited spatial coverage, we coarsened the mesh and extracted data within 50
448 km of the aircraft. At the same time, extracting the average value from coarse cells will decrease
449 the numerical values of EDR. So when half of the cells in this rough cell can reach the value
450 of turbulence ($EDR > 0.1$), the maximum values are selected, otherwise, the average values are
451 selected. For each time point of a report, the best member or average of members is selected from
452 six members. Moreover, only Case 1, 2, and 5, where MPAS has good performance, are used.
453 Figure 11 shows the analysis. Overall, SFSR has a significantly higher value in the correlation
454 coefficient. Specifically, SFSR has higher values of EDR than 2ndSF. In the low EDR region
455 ($0 \sim 0.1$), the overall values of SFSR are higher. In region with turbulence, the EDR values from
456 SFSR are closer to the observation. Although SFSR and 2ndSF are lower for extreme turbulence,
457 SFSR has higher values. Therefore, SFSR performs better in predicting the intensity of turbulence.
458 In Figure 11 b, the values of higher EDR are decreased because we took the unweighted average,
459 while overestimation is evident in the low EDR region. Hence, the correlation coefficients in both
460 methods are very low. It indicates that extracting the unweighted average of members is not an
461 optimal method to do the predictions.

462 The results also show the difference in POD and FA between SFSR and 2ndSF. The Relative
463 operating characteristic (ROC) curves in Fig.11 c can reflect that these two methods are superior
464 to random guesses and better performance of SFSR with a larger area under the curve (AUC).
465 Meanwhile, similar to Fig.11 b, the AUCs of both methods in Fig.11 d have significantly decreased.
466 Although SFSR performs better, its AUC is only slightly higher than 0.5, which is not very valuable
467 in predicting turbulence by extracting average values. As for the observations out of airplanes, in
468 comparison with GTG3, it was found that SFSR performs better in spatial distribution. Therefore,
469 whether it is a large-scale horizontal distribution or a comparison with the in-situ observations
470 from the aircraft, SFSR performs better and is a more effective method.

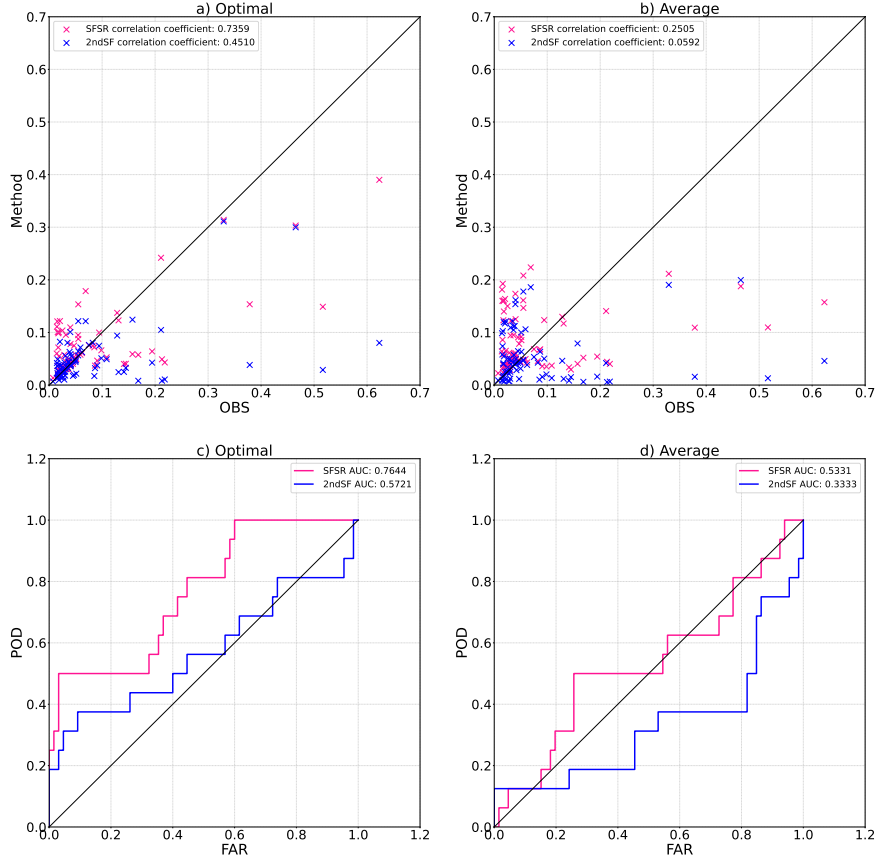


FIG. 11. Scatter plots of the EDR between observation (X-axis) and two methods (Y-axis) and ROC curves from Case 1, 2, and 5. Curves are constructed based on two methods with an observational threshold of $EDR = 0.1 \text{ m}^2/3 \text{ s}^{-1}$. When half of the cells in the coarse cell reach turbulence, the maximum values are selected, and if there is no report, the average value is selected. For a time point of a report, the optimal members were selected from six members in a) and c), while the averages of members were selected in b) and d).

7. Summary and Discussion

This study uses the non-hydrostatic, variable-resolution MPAS to predict convectively induced turbulence. The MPAS mesh uses 60-km resolution for most parts of the world but has a refined 3-km resolution region that covers the South China continent and the South China Sea and is centered in Hong Kong. We compared three methods to calculate EDR, an aircraft-independent measure of turbulence intensity, from convection-permitting simulation output. The new method employs the framework of explicit filtering and reconstruction in large eddy simulations turbulence modelling and estimates resolvable subfilter-scale TKE, which is then used to calculate EDR. This new method outperforms the previous estimation method using the second-order structure functions method and the convective gravity wave drag with its more accurate prediction of turbulence intensity and

486 spatial distribution. The new method’s predictions agree more with the GTG3 product because of
487 similar spatial pattern of turbulence.

488 Because the new method relies on resolved velocity field to estimate TKE, we also assessed its
489 dependency on MPAS resolution. Testing with refined region resolution of 1, 3, 9, and 18 km
490 shows that higher resolution simulations provide better EDR estimation regarding both intensity
491 and spatial coverage. However, increasing the resolution also substantially increases computational
492 costs. The 3-km resolution appears to be a balanced choice considering the trade-off between
493 accuracy and computational resource demand. Thus, we use it for other simulations in our study.

494 Convection-permitting resolutions are in the gray zone for turbulence and convection param-
495 eterization. Therefore, the choice of relevant physical and numerical options is a fundamental
496 source of uncertainty in the prediction of convectively induced turbulence. We examined some
497 available scheme variations in MPAS and found such a physical perturbation-based ensemble ef-
498 fectively captures some convection stochasticity. However, among those variations, the choice of
499 microphysics and cumulus convection schemes exhibit more impact on the predicted convection.
500 Compared to the Thompson microphysics scheme, WSM6 led to earlier convection initiation and
501 peaking and higher cloud tops. Switching off the scale-aware GF convection scheme resulted in
502 more intense turbulence and a prolonged convective system. Furthermore, we have observed a
503 strong correlation between the intensity and evolution of turbulence with convection, emphasizing
504 the necessity of accurate simulations in convection for turbulence forecasting.

505 Further testing with more CIT cases showed that both the distribution and maximum values of
506 EDR, SFSR can provide closer results to observations and similar statistics properties with the
507 previous studies, while extreme EDR values should be calibrated. SFSR shows significantly higher
508 correlation coefficient than 2ndSF between observations. And they have almost same POD and
509 FA. More observations should be included to solve the avoidance bias to make them different in
510 statistics and to select thresholds of turbulence for SFSR in 3-km mesh by mapping (Sharman and
511 Pearson 2017).

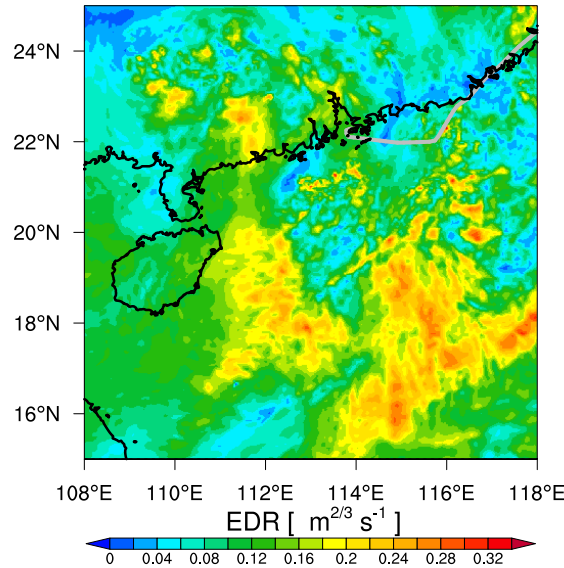
512 For some convective systems, significant location bias exists in the convection-permitting sim-
513 ulations, and the physical perturbation-based ensemble has its limitation in generating enough
514 ensemble spread. We will test the effectiveness of initial condition perturbation-based ensemble
515 and related post-processing methods to provide accurate predictions in the future.

516 *Acknowledgments.* The project is part of the Aviation Research and Development Project Phase 2
 517 (AvRDP2), supported by World Meteorological Organization. The authors thank HKUST Fok Ying
 518 Tung Research Institute and National Supercomputing Center in Guangzhou Nansha sub-center for
 519 providing high performance computational resources.

520 *Data availability statement.* The release version of MPAS-Atmosphere can be down-
 521 loaded from <https://doi.org/10.5281/zenodo.4892293>. The technology to gener-
 522 ate the meshes can be found in [http://mpas-dev.github.io/MPAS-Tools/stable/](http://mpas-dev.github.io/MPAS-Tools/stable/mesh_creation.html#building-a-jigsaw-mesh)
 523 [mesh_creation.html#building-a-jigsaw-mesh](http://mpas-dev.github.io/MPAS-Tools/stable/mesh_creation.html#building-a-jigsaw-mesh). The ERA5 data can be down-
 524 loaded on [https://cds.climate.copernicus.eu/cdsapp#!/dataset/10.24381/cds.](https://cds.climate.copernicus.eu/cdsapp#!/dataset/10.24381/cds.bd0915c6?tab=overview)
 525 [bd0915c6?tab=overview](https://cds.climate.copernicus.eu/cdsapp#!/dataset/10.24381/cds.bd0915c6?tab=overview). The namelist file and codes to calculate the EDR with different
 526 methods can be found in <https://doi.org/10.5281/zenodo.8092926>.

527 APPENDIX A

528 Filtering on Hexagon Mesh



529 FIG. A1. Spatial distributions of the EDR of Case 1 at May 21, 2020 01:50 a.m. at the altitude of 10 km.
 530 Applying the subfilter-scale reconstruction method in original hexagon mesh. The gray line represents the route
 531 of the airplane in Case 3 in Table 1, the details about the turbulence are in Fig. 1.

The Influence of WSM6 to Cloud Top Height

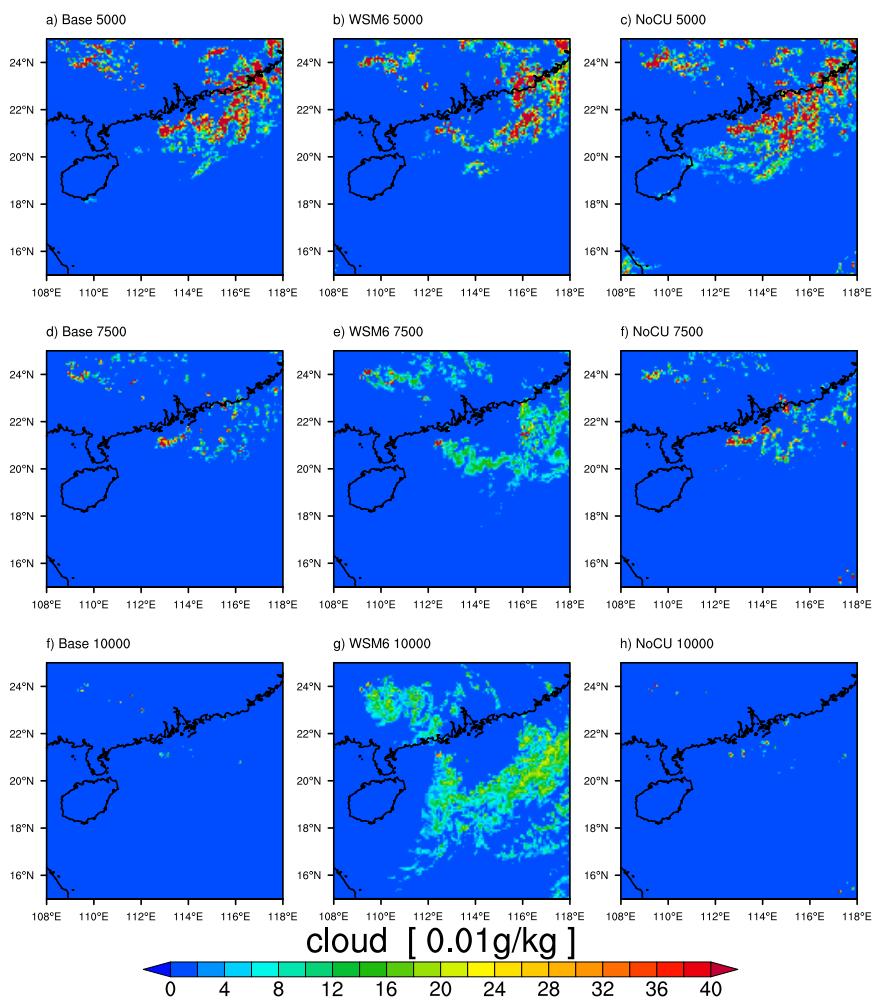


FIG. B1. Spatial distributions of the cloud in different altitudes with different options at May 21, 2020 01:50 a.m.

References

- Ahmad, N., and F. Proctor, 2012: *Estimation of Eddy Dissipation Rates from Mesoscale Model Simulations*. <https://doi.org/10.2514/6.2012-429>.
- Allen, J., 2005: Perfect Reconstruction Filter Banks for the Hexagon Grid. *2005 5th International Conference on Information Communications & Signal Processing*, IEEE, Bangkok, Thailand, 73–76, <https://doi.org/10.1109/ICICS.2005.1689007>.
- Barber, K. A., W. Deierling, G. Mullendore, C. Kessinger, R. Sharman, and D. Muñoz-Esparza, 2019: Properties of Convectively Induced Turbulence over Developing Oceanic Convection. *Monthly Weather Review*, **147** (9), 3429–3444, <https://doi.org/10.1175/MWR-D-18-0409.1>.
- Bell, B., and Coauthors, 2021: The ERA5 global reanalysis: Preliminary extension to 1950. *Quarterly Journal of the Royal Meteorological Society*, **147** (741), 4186–4227, <https://doi.org/10.1002/qj.4174>.
- Bouttier, F., B. Vié, O. Nuissier, and L. Raynaud, 2012: Impact of Stochastic Physics in a Convection-Permitting Ensemble. *Monthly Weather Review*, **140** (11), 3706–3721, <https://doi.org/10.1175/MWR-D-12-00031.1>.
- Brown, D., R. Brownrigg, M. Haley, and W. Huang, 2012: NCAR Command Language (NCL). UCAR/NCAR - Computational and Information Systems Laboratory (CISL), <https://doi.org/10.5065/D6WD3XH5>.
- Chen, F., and J. Dudhia, 2001: Coupling an Advanced Land Surface–Hydrology Model with the Penn State–NCAR MM5 Modeling System. Part I: Model Implementation and Sensitivity. *Monthly Weather Review*, **129** (4), 569–585, [https://doi.org/10.1175/1520-0493\(2001\)129\(0569:CAALSH\)2.0.CO;2](https://doi.org/10.1175/1520-0493(2001)129(0569:CAALSH)2.0.CO;2).
- Chow, F. K., R. L. Street, M. Xue, and J. H. Ferziger, 2005: Explicit Filtering and Reconstruction Turbulence Modeling for Large-Eddy Simulation of Neutral Boundary Layer Flow. *Journal of the Atmospheric Sciences*, **62** (7), 2058–2077, <https://doi.org/10.1175/JAS3456.1>.
- DUTTON, MJO., 1980: PROBABILITY FORECASTS OF CLEAR-AIR TURBULENCE BASED ON NUMERICAL MODEL OUTPUT. *PROBABILITY FORECASTS OF CLEAR-AIR TURBULENCE BASED ON NUMERICAL MODEL OUTPUT*.

- 562 Ellrod, G. P., and J. A. Knox, 2010: Improvements to an Operational Clear-Air Turbulence
563 Diagnostic Index by Addition of a Divergence Trend Term. *Weather and Forecasting*, **25** (2),
564 789–798, <https://doi.org/10.1175/2009WAF2222290.1>.
- 565 Endlich, R. M., 1964: The Mesoscale Structure of Some Regions of Clear-Air Turbulence. *Journal*
566 *of Applied Meteorology*, **3** (3), 261–276, [https://doi.org/10.1175/1520-0450\(1964\)003<0261:](https://doi.org/10.1175/1520-0450(1964)003<0261:TMSOSR>2.0.CO;2)
567 [TMSOSR](https://doi.org/10.1175/1520-0450(1964)003<0261:TMSOSR>2.0.CO;2)2.0.CO;2.
- 568 Frehlich, R., and R. Sharman, 2004: Estimates of Turbulence from Numerical Weather Prediction
569 Model Output with Applications to Turbulence Diagnosis and Data Assimilation. *Monthly*
570 *Weather Review*, **132** (10), 2308–2324, [https://doi.org/10.1175/1520-0493\(2004\)132<2308:](https://doi.org/10.1175/1520-0493(2004)132<2308:EOTFNW>2.0.CO;2)
571 [EOTFNW](https://doi.org/10.1175/1520-0493(2004)132<2308:EOTFNW>2.0.CO;2)2.0.CO;2.
- 572 Frehlich, R., and R. Sharman, 2010: Climatology of Velocity and Temperature Turbulence Statistics
573 Determined from Rawinsonde and ACARS/AMDAR Data. *Journal of Applied Meteorology and*
574 *Climatology*, **49** (6), 1149–1169, <https://doi.org/10.1175/2010JAMC2196.1>.
- 575 Grell, G. A., and S. R. Freitas, 2014: A scale and aerosol aware stochastic convective parame-
576 terization for weather and air quality modeling. *Atmospheric Chemistry and Physics*, **14** (10),
577 5233–5250, <https://doi.org/10.5194/acp-14-5233-2014>.
- 578 Gullbrand, J., and F. K. Chow, 2003: The effect of numerical errors and turbulence models in
579 large-eddy simulations of channel flow, with and without explicit filtering. *Journal of Fluid*
580 *Mechanics*, **495**, 323–341, <https://doi.org/10.1017/S0022112003006268>.
- 581 Hagos, S., L. R. Leung, Q. Yang, C. Zhao, and J. Lu, 2015: Resolution and Dynamical Core
582 Dependence of Atmospheric River Frequency in Global Model Simulations. *Journal of Climate*,
583 **28** (7), 2764–2776, <https://doi.org/10.1175/JCLI-D-14-00567.1>.
- 584 Hersbach, H., and Coauthors, 2020: The ERA5 global reanalysis. *Quarterly Journal of the Royal*
585 *Meteorological Society*, **146** (730), 1999–2049, <https://doi.org/10.1002/qj.3803>.
- 586 Hong, S.-Y., 2010: A new stable boundary-layer mixing scheme and its impact on the simulated
587 East Asian summer monsoon. *Quarterly Journal of the Royal Meteorological Society*, **136** (651),
588 1481–1496, <https://doi.org/10.1002/qj.665>.

- 589 Hong, S.-Y., J.-h. Kim, J.-o. Lim, and J. Dudhia, 2006: The WRF single moment microphysics
590 scheme (WSM). *Journal of the Korean Meteorological Society*, **42**, 129–151.
- 591 Iacono, M. J., E. J. Mlawer, S. A. Clough, and J.-J. Morcrette, 2000: Impact of an improved
592 longwave radiation model, RRTM, on the energy budget and thermodynamic properties of the
593 NCAR community climate model, CCM3. *Journal of Geophysical Research: Atmospheres*,
594 **105 (D11)**, 14 873–14 890, <https://doi.org/10.1029/2000JD900091>.
- 595 Jang, W., H.-Y. Chun, and J.-H. Kim, 2009: A Study of Forecast System for Clear-Air Turbulence
596 in Korea Part I: Korean Integrated Turbulence Forecasting Algorithm (KITFA). *Atmosphere*,
597 **19 (3)**, 255–268.
- 598 Kim, S.-H., and H.-Y. Chun, 2016: Aviation turbulence encounters detected from aircraft observa-
599 tions: Spatiotemporal characteristics and application to Korean Aviation Turbulence Guidance:
600 Aviation turbulence encounters detected from aircraft observations. *Meteorological Applica-*
601 *tions*, **23 (4)**, 594–604, <https://doi.org/10.1002/met.1581>.
- 602 Kim, S.-H., H.-Y. Chun, R. D. Sharman, and S. B. Trier, 2019: Development of Near-
603 Cloud Turbulence Diagnostics Based on a Convective Gravity Wave Drag Parameteriza-
604 tion. *Journal of Applied Meteorology and Climatology*, **58 (8)**, 1725–1750, [https://doi.org/](https://doi.org/10.1175/JAMC-D-18-0300.1)
605 [10.1175/JAMC-D-18-0300.1](https://doi.org/10.1175/JAMC-D-18-0300.1).
- 606 Kolmogorov, A. N., 1991: The Local Structure of Turbulence in Incompressible Viscous Fluid for
607 Very Large Reynolds Numbers. *Proceedings: Mathematical and Physical Sciences*, **434 (1890)**,
608 9–13, 51980.
- 609 Landu, K., L. R. Leung, S. Hagos, V. Vinoj, S. A. Rauscher, T. Ringler, and M. Taylor, 2014:
610 The Dependence of ITCZ Structure on Model Resolution and Dynamical Core in Aquaplanet
611 Simulations. *Journal of Climate*, **27 (6)**, 2375–2385, [https://doi.org/10.1175/JCLI-D-13-00269.](https://doi.org/10.1175/JCLI-D-13-00269.1)
612 [1.](https://doi.org/10.1175/JCLI-D-13-00269.1)
- 613 Lane, T. P., J. D. Doyle, R. D. Sharman, M. A. Shapiro, and C. D. Watson, 2009: Statistics
614 and Dynamics of Aircraft Encounters of Turbulence over Greenland. *Monthly Weather Review*,
615 **137 (8)**, 2687–2702, <https://doi.org/10.1175/2009MWR2878.1>.

- 616 Lane, T. P., and R. D. Sharman, 2014: Intensity of thunderstorm-generated turbulence revealed
617 by large-eddy simulation. *Geophysical Research Letters*, **41** (6), 2221–2227, [https://doi.org/](https://doi.org/10.1002/2014GL059299)
618 10.1002/2014GL059299.
- 619 Lane, T. P., R. D. Sharman, T. L. Clark, and H.-M. Hsu, 2003: An Investigation of Turbulence
620 Generation Mechanisms above Deep Convection. *Journal of the Atmospheric Sciences*, **60** (10),
621 1297–1321, [https://doi.org/10.1175/1520-0469\(2003\)60<1297:AIOTGM>2.0.CO;2](https://doi.org/10.1175/1520-0469(2003)60<1297:AIOTGM>2.0.CO;2).
- 622 Li, G., H. Chen, M. Xu, C. Zhao, L. Zhong, R. Li, Y. Fu, and Y. Gao, 2022: Impacts of
623 Topographic Complexity on Modeling Moisture Transport and Precipitation over the Tibetan
624 Plateau in Summer. *Advances in Atmospheric Sciences*, **39**, 1151–1166, [https://doi.org/10.1007/](https://doi.org/10.1007/s00376-022-1409-7)
625 s00376-022-1409-7.
- 626 Lindborg, E., 1999: Can the atmospheric kinetic energy spectrum be explained by two-
627 dimensional turbulence? *Journal of Fluid Mechanics*, **388**, 259–288, [https://doi.org/10.1017/](https://doi.org/10.1017/S0022112099004851)
628 S0022112099004851.
- 629 Min, K.-H., S. Choo, D. Lee, and G. Lee, 2015: Evaluation of WRF Cloud Microphysics Schemes
630 Using Radar Observations. *Weather and Forecasting*, **30** (6), 1571–1589, [https://doi.org/10.](https://doi.org/10.1175/WAF-D-14-00095.1)
631 1175/WAF-D-14-00095.1.
- 632 Mingyue, x., and Coauthors, 2021: Convection-Permitting Hindcasting of Diurnal Variation of
633 Mei-yu Rainfall Over East China With a Global Variable-Resolution Model. *Journal of Geo-*
634 *physical Research: Atmospheres*, **126**, <https://doi.org/10.1029/2021JD034823>.
- 635 Mlawer, E. J., S. J. Taubman, P. D. Brown, M. J. Iacono, and S. A. Clough, 1997: Radiative transfer
636 for inhomogeneous atmospheres: RRTM, a validated correlated-k model for the longwave.
637 *Journal of Geophysical Research: Atmospheres*, **102** (D14), 16 663–16 682, [https://doi.org/](https://doi.org/10.1029/97JD00237)
638 10.1029/97JD00237.
- 639 Mohan, P. R., C. V. Srinivas, V. Yesubabu, R. Baskaran, and B. Venkatraman, 2019: Tropical
640 cyclone simulations over Bay of Bengal with ARW model: Sensitivity to cloud microphysics
641 schemes. *Atmospheric Research*, **230**, 104 651, <https://doi.org/10.1016/j.atmosres.2019.104651>.
- 642 Monin, A. S., and A. M. Yaglom, 2013: *Statistical Fluid Mechanics, Volume II: Mechanics of*
643 *Turbulence*. Courier Corporation.

- 644 Muñoz-Esparza, D., and B. Kosović, 2018: Generation of Inflow Turbulence in Large-Eddy
645 Simulations of Nonneutral Atmospheric Boundary Layers with the Cell Perturbation Method.
646 *Monthly Weather Review*, **146** (6), 1889–1909, <https://doi.org/10.1175/MWR-D-18-0077.1>.
- 647 Muñoz-Esparza, D., R. Sharman, J. Sauer, and B. Kosović, 2018: Toward Low-Level Turbu-
648 lence Forecasting at Eddy-Resolving Scales. *Geophysical Research Letters*, **45** (16), 8655–8664,
649 <https://doi.org/10.1029/2018GL078642>.
- 650 Muñoz-Esparza, D., R. D. Sharman, and W. Deierling, 2020: Aviation Turbulence Forecasting at
651 Upper Levels with Machine Learning Techniques Based on Regression Trees. *Journal of Applied*
652 *Meteorology and Climatology*, **59** (11), 1883–1899, [https://doi.org/10.1175/JAMC-D-20-0116](https://doi.org/10.1175/JAMC-D-20-0116.1).
653 1.
- 654 Nakanishi, M., and H. Niino, 2009: Development of an Improved Turbulence Closure Model for
655 the Atmospheric Boundary Layer. *Journal of the Meteorological Society of Japan. Ser. II*, **87** (5),
656 895–912, <https://doi.org/10.2151/jmsj.87.895>.
- 657 Nastrom, G. D., and K. S. Gage, 1985: A Climatology of Atmospheric Wavenumber Spectra of
658 Wind and Temperature Observed by Commercial Aircraft. *Journal of the Atmospheric Sciences*,
659 **42** (9), 950–960, [https://doi.org/10.1175/1520-0469\(1985\)042<0950:ACOAWS>2.0.CO;2](https://doi.org/10.1175/1520-0469(1985)042<0950:ACOAWS>2.0.CO;2).
- 660 O’Brien, T. A., F. Li, W. D. Collins, S. A. Rauscher, T. D. Ringler, M. Taylor, S. M. Hagos, and L. R.
661 Leung, 2013: Observed Scaling in Clouds and Precipitation and Scale Incognizance in Regional
662 to Global Atmospheric Models. *Journal of Climate*, **26** (23), 9313–9333, [https://doi.org/10](https://doi.org/10.1175/JCLI-D-13-00005.1).
663 1175/JCLI-D-13-00005.1.
- 664 Sakaguchi, K., and Coauthors, 2015: Exploring a Multiresolution Approach Using AMIP Simula-
665 tions. *Journal of Climate*, **28** (14), 5549–5574, <https://doi.org/10.1175/JCLI-D-14-00729.1>.
- 666 Schumann, U., 1991: Subgrid length-scales for large-eddy simulation of stratified turbu-
667 lence. *Theoretical and Computational Fluid Dynamics*, **2** (5), 279–290, [https://doi.org/](https://doi.org/10.1007/BF00271468)
668 10.1007/BF00271468.
- 669 Sharman, R., and T. Lane, Eds., 2016: *Aviation Turbulence*. Springer International Publishing,
670 Cham, <https://doi.org/10.1007/978-3-319-23630-8>.

671 Sharman, R., C. Tebaldi, G. Wiener, and J. Wolff, 2006: An Integrated Approach to Mid- and
672 Upper-Level Turbulence Forecasting. *Weather and Forecasting*, **21** (3), 268–287, [https://doi.org/](https://doi.org/10.1175/WAF924.1)
673 10.1175/WAF924.1.

674 Sharman, R. D., L. B. Cornman, G. Meymaris, J. Pearson, and T. Farrar, 2014: Description
675 and Derived Climatologies of Automated In Situ Eddy-Dissipation-Rate Reports of Atmo-
676 spheric Turbulence. *Journal of Applied Meteorology and Climatology*, **53** (6), 1416–1432,
677 <https://doi.org/10.1175/JAMC-D-13-0329.1>.

678 Sharman, R. D., J. D. Doyle, and M. A. Shapiro, 2012: An Investigation of a Commercial
679 Aircraft Encounter with Severe Clear-Air Turbulence over Western Greenland. *Journal of Applied*
680 *Meteorology and Climatology*, **51** (1), 42–53, <https://doi.org/10.1175/JAMC-D-11-044.1>.

681 Sharman, R. D., and J. M. Pearson, 2017: Prediction of Energy Dissipation Rates for Aviation
682 Turbulence. Part I: Forecasting Nonconvective Turbulence. *Journal of Applied Meteorology and*
683 *Climatology*, **56** (2), 317–337, <https://doi.org/10.1175/JAMC-D-16-0205.1>.

684 Shi, X., F. K. Chow, R. L. Street, and G. H. Bryan, 2019: Key Elements of Turbulence Closures for
685 Simulating Deep Convection at Kilometer-Scale Resolution. *Journal of Advances in Modeling*
686 *Earth Systems*, **11** (3), 818–838, <https://doi.org/10.1029/2018MS001446>.

687 Shi, X., and Y. Wang, 2022: Impacts of Cumulus Convection and Turbulence Parameterizations
688 on the Convection-Permitting Simulation of Typhoon Precipitation. *Monthly Weather Review*,
689 **150** (11), 2977–2997, <https://doi.org/10.1175/MWR-D-22-0057.1>.

690 Skamarock, W. C., 2004: Evaluating Mesoscale NWP Models Using Kinetic Energy Spectra.
691 *Monthly Weather Review*, **132** (12), 3019–3032, <https://doi.org/10.1175/MWR2830.1>.

692 Skamarock, W. C., J. B. Klemp, M. G. Duda, L. D. Fowler, S.-H. Park, and T. D. Ringler,
693 2012: A Multiscale Nonhydrostatic Atmospheric Model Using Centroidal Voronoi Tessellations
694 and C-Grid Staggering. *Monthly Weather Review*, **140** (9), 3090–3105, [https://doi.org/10.1175/](https://doi.org/10.1175/MWR-D-11-00215.1)
695 MWR-D-11-00215.1.

696 Skamarock, W. C., S.-H. Park, J. B. Klemp, and C. Snyder, 2014: Atmospheric Kinetic Energy
697 Spectra from Global High-Resolution Nonhydrostatic Simulations. *Journal of the Atmospheric*
698 *Sciences*, **71** (11), 4369–4381, <https://doi.org/10.1175/JAS-D-14-0114.1>.

699 Takacs, A., L. Holland, R. Hueftle, B. Brown, and A. Holmes, 2005: Using in situ eddy dissipation
700 rate (EDR) observations for turbulence forecast verification.

701 Thompson, G., P. R. Field, R. M. Rasmussen, and W. D. Hall, 2008: Explicit Forecasts of
702 Winter Precipitation Using an Improved Bulk Microphysics Scheme. Part II: Implementation of
703 a New Snow Parameterization. *Monthly Weather Review*, **136** (12), 5095–5115, [https://doi.org/](https://doi.org/10.1175/2008MWR2387.1)
704 10.1175/2008MWR2387.1.

705 Trier, S. B., and R. D. Sharman, 2016: Mechanisms Influencing Cirrus Banding and Aviation
706 Turbulence near a Convectively Enhanced Upper-Level Jet Stream. *Monthly Weather Review*,
707 **144** (8), 3003–3027, <https://doi.org/10.1175/MWR-D-16-0094.1>.

708 Trier, S. B., R. D. Sharman, R. G. Fovell, and R. G. Frehlich, 2010: Numerical Simulation of Radial
709 Cloud Bands within the Upper-Level Outflow of an Observed Mesoscale Convective System.
710 *Journal of the Atmospheric Sciences*, **67** (9), 2990–2999, [https://doi.org/10.1175/2010JAS3531](https://doi.org/10.1175/2010JAS3531.1).
711 1.

712 Tvaryanas, A. P., 2003: Epidemiology of Turbulence-Related Injuries in Airline Cabin Crew,
713 1992–2001. *Aviation, Space, and Environmental Medicine*, **74** (9), 970–976.

714 Vinnichenko, N., 2013: *Turbulence in the Free Atmosphere*. Springer Science & Business Media.

715 Vogel, G., and C. Sampson, 1996: Clear Air Turbulence Indices Derived from U.S. Navy Numerical
716 Model Data: A Verification Study. 34.

717 Yang, Q., L. R. Leung, S. A. Rauscher, T. D. Ringler, and M. A. Taylor, 2014: Atmospheric Moisture
718 Budget and Spatial Resolution Dependence of Precipitation Extremes in Aquaplanet Simulations.
719 *Journal of Climate*, **27** (10), 3565–3581, <https://doi.org/10.1175/JCLI-D-13-00468.1>.

720 Zhao, C., and Coauthors, 2016: Exploring the impacts of physics and resolution on aqua-planet sim-
721 ulations from a nonhydrostatic global variable-resolution modeling framework. *Journal of Ad-
722 vances in Modeling Earth Systems*, **8** (4), 1751–1768, <https://doi.org/10.1002/2016MS000727>.